OPEN ACCESS
IOP Publishing
Measurement Science and Technology
Meas. Sci. Technol. **34** (2023) 125204 (12pp)
https://doi.org/10.1088/1361-6501/acf334

Low-coherence and broadband confocal refractometry: reducing the measurement time

D Francis*, J M Hallam and R P Tatam

Engineering Photonics, Cranfield University, Cranfield, Bedfordshire, MK43 0AL, United Kingdom

E-mail: daniel.francis@cranfield.ac.uk

Received 30 January 2023, revised 17 August 2023
Accepted for publication 23 August 2023
Published 4 September 2023

Abstract

This paper describes the steps taken to improve the measurement speed of a combined low-coherence and confocal refractive index measurement system. The instrument measures the refractive index and thickness of transparent plates using a fibre-based low-coherence interferometer with a line-scan spectrometer. The spectrometer allows on-line dispersion measurement which is necessary to derive the sample thickness t as well as both the phase and group refractive indices n_p, n_g. The measurements were performed on a sample with six surfaces consisting of three glass windows mounted in a lens tube. Experimental results show that a measurement time of 4.4 s for the multi-layered object, which has a total thickness of approximately 10.5 mm, can be achieved whilst maintaining an accuracy of better than 0.1% for n_p, n_g, and t. This represents an approximately hundredfold improvement over previously published measurements.

Supplementary material for this article is available online

Keywords: confocal, refractometry, refractive index measurement, low-coherence interferometry, dispersion, peak detection

(Some figures may appear in colour only in the online journal)

1. Introduction

The use of interferometric techniques for measuring the thickness and refractive index of transparent media has generated significant interest in recent years [1–9]. Of these, one of the most popular is low-coherence interferometry (LCI) which can be used for measuring distances from the micro to millimetre scale. It has been shown that the refractive index of the medium between pairs of reflective interfaces can be measured by scanning the focus of an optical coherence tomography system (OCT) through the interfaces [10, 11]. Low-coherence techniques, including OCT, measure the optical distance, which is the product of the physical layer thickness t and the group refractive index n_g. Therefore, when using LCI to measure refractive index, it is n_g that is derived, rather than the phase index n_p. To derive both n_p and t an additional measurement is required, and this has led to the combination of LCI with confocal scanning.

Early research into the combination of these two techniques looked at optimising the measurement for n_p and t [12–15]. Interest then focused on adaptations enabling the measurement of all three parameters n_g, n_p, and t. These adaptations utilized either sophisticated sample mounting apparatus [16] or approximated derivations of the chromatic dispersion of

* Author to whom any correspondence should be addressed.

Original content from this work may be used under the terms of the Creative Commons Attribution 4.0 licence. Any further distribution of this work must maintain attribution to the author(s) and the title of the work, journal citation and DOI.

 © 2023 The Author(s). Published by IOP Publishing Ltd

index $dn_p/d\lambda$ [17, 18]. The work of Kim *et al* [19] showed that these three parameters could be calculated by making the confocal measurement at multiple wavelengths. This was done by repeating the measurement using three different optical sources to measure the dispersion of the confocal parameter. Our previous work [20] demonstrated a similar multi-wavelength approach which instead used a line-scan spectrometer to make the confocal dispersion measurement at higher resolution with a single confocal scan. In addition to enabling the measurement of all three parameters, this combination of techniques also allows for much larger layer thicknesses to be measured than with LCI alone, which is limited to the Rayleigh range of the focusing lens.

More recent research has focused on expanding the technique, for example adding multi-dimensionality [5], or enabling simultaneous acquisition of the confocal and low-coherence parameters. Simultaneous acquisition has been done either by concatenating interferometers [21], or by acquiring the confocal data through chromatic dispersion of focus [2]. Other research has expanded the range of applications of the technique, for example applying it to graded index materials [1, 21], opaque materials [22], compound optics [3] and multi-lens arrays [23], or contact lenses [24]. The use of frequency-domain [25] or swept-source [1, 5, 26] LCI can help to simplify the system and remove the need for moving parts leading to better stability and faster measurements, at the cost of the ability to measure n_p.

Improving the measurement speed is highly beneficial for biological samples or any situation where either the ambient or sample conditions may change over the duration of a scan, as well as from increasing the throughput of measured samples. This paper aims to describe the steps taken to improve the measurement speed by approximately two orders of magnitude over the those presented in [20], whilst retaining an accuracy of better than 0.1%. Reducing the measurement time is achieved by increasing the travel speed of the translation stages, particularly for the confocal scan, which consists of a single translation of the sample through the beam focus. Increasing the scan speed raises several issues related to data acquisition, peak detection, and peak localization, which are discussed in subsequent sections in the paper. The result of the changes is a measurement time that is less than 0.5 s per millimetre of sample thickness, for a sample that is ~10.5 mm thick. This represents an improvement on the ~10 s per element reported in [19] and is comparable to the ~1 s for the sub-millimetre sample reported in [21], which relies on simultaneous detection of the confocal and low-coherence signals using dual interferometers and is limited to thin (<1 mm) objects.

2. Interferometer configuration and measurement principles

A schematic of the interferometer used in this work is shown in figure 1. The source is a 50 nm bandwidth super-luminescent diode (SLD) centred at 840 nm with an optical power of 10 mW, that is a constituent of the Superlum M-T-850-HP-I Broadlighter system. Light from the source is ported to a fibre-optic coupler (Thorlabs TW850R2A2), which has a bandwidth of 850 ± 100 nm. In this system, the 4.4 μm diameter fibre core acts as the confocal aperture. The translation stages are a pair of Physik Instrumente (PI) V408 linear stages which provide a travel range of 50 mm, a maximum velocity of 500 mm·s^{-1}, and a minimum incremental motion of 20 nm. The stages are controlled using a pair of C-891 stage controllers. The spectrometer connected to the return leg of the coupler is a Bayspec OCT spectrograph @850 which has an approximate bandwidth of 50 nm. Calibration of the spectrometer was achieved using a tungsten halogen lamp with a grating and slit monochromator and the procedure is described in more detail in [20]. The spectrometer incorporates a Basler spL4096-140 km line-scan CMOS camera which has an array size of 4096 pixels, 12-bit digital resolution, and a maximum single-line acquisition rate of 70 kHz. No dead pixels have been observed in the array during this work. The camera is interfaced to a PC using a National Instruments (NI) PCIe-1433 full Camera-Link frame grabber. A pair of off-axis parabolic (OAP) mirrors are used to collimate and focus light in the sample arm of the interferometer. The focal lengths of the collimation and focusing mirrors are 25.4 mm and 50.8 mm respectively. We previously showed that a significant improvement in performance can be obtained using OAP mirrors instead of comparative lens systems due to the reduced impact of optical aberrations [27]. The main impact of optical aberrations here is that they can distort the dispersion curve often to the extent that the gradient, needed for the refractive index calculation, is completely obscured. Optical aberration is less of an issue in the interferometric measurement hence the reference channel can use a simpler optical design with achromatic doublet lenses which allows for a more compact optical system. The reference arm of the interferometer is formed by a mirror mounted on the second translation stage and a shutter (Thorlabs SHB05T) in the reference arm is used to block light from the reference mirror when making the confocal measurements. The shutter is controlled using an NI 9263 analog output module housed in an NI cDAQ-9174 chassis.

Scanning a transparent planar object so that each of its interfaces passes through the focus results in a series of reflection peaks in the integrated signal of the spectrometer. For a single element window with two interfaces, this is a pair of peaks that are separated by a quantity Δz that is related to the thickness t and phase index n_p by [16]

$$\Delta z = t \times \frac{\sqrt{(1-NA^2)}}{\sqrt{(n_p^2-NA^2)}} \approx \frac{t}{n_p} \tag{1}$$

where NA is the numerical aperture of the focusing optics in the sample arm. The width of the peaks is dependent on the NA of the optics and the diameter of the confocal aperture. The NA of the system shown in figure 1 is 0.061. An example of a pair of confocal peaks obtained from a 2.161 mm thick BK7 glass

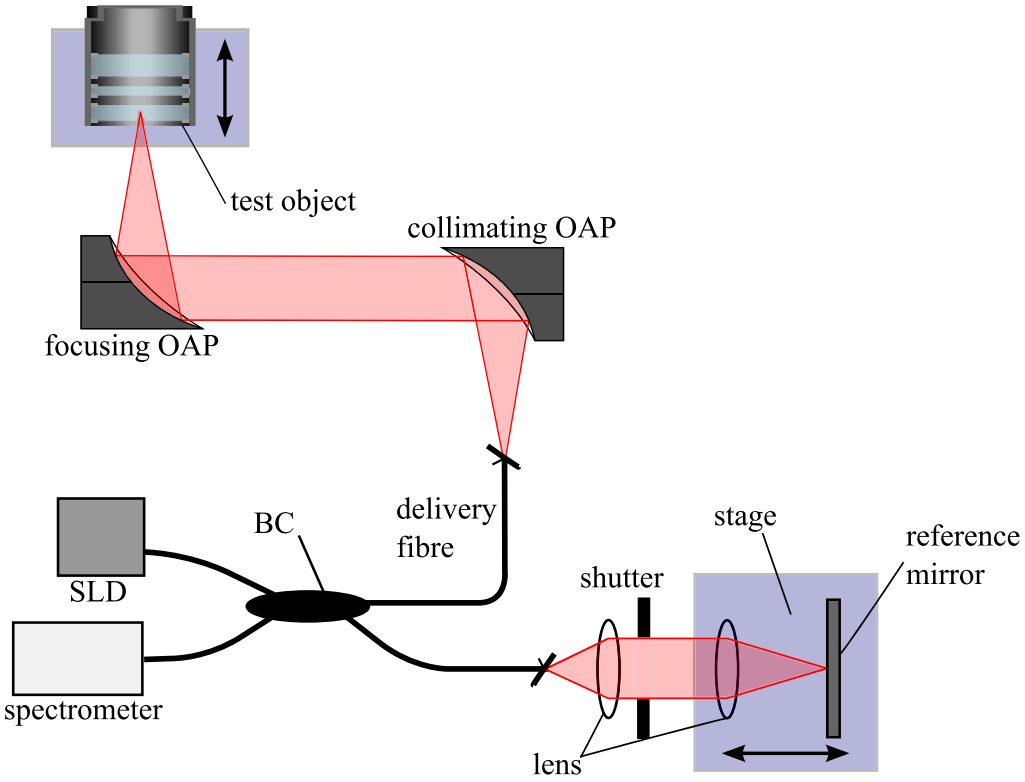

Figure 1. Schematic showing the configuration of the interferometer. SLD—superluminescent diode; BC—broadband coupler; OAP—off-axis parabolic mirror. The light blue shading shows the translation stages and indicates the components that are mounted on them.

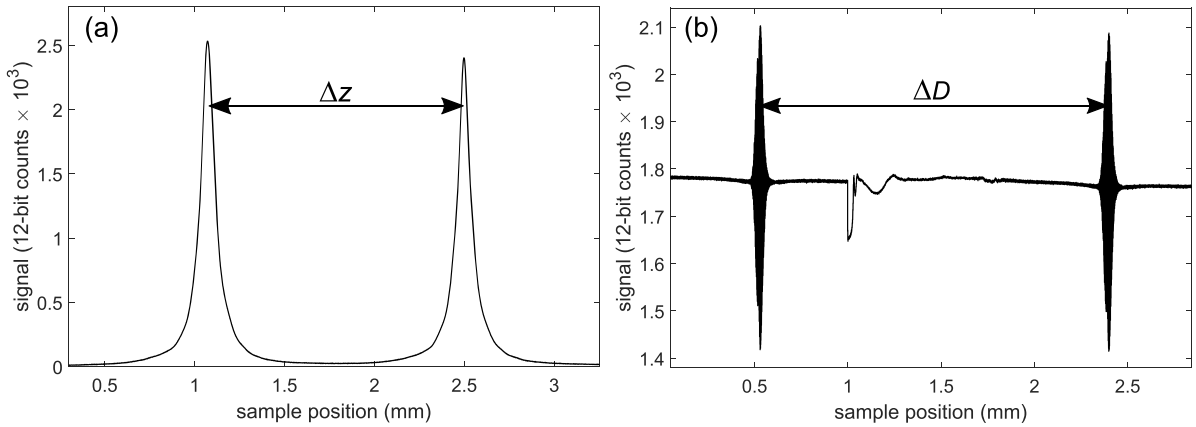

Figure 2. Plots showing (a) the confocal peaks observed in the integrated spectrometer signal separated by $\Delta z = 1.425$ mm, and (b), the low-coherence fringe envelopes separated by $\Delta D = 1.868$ mm. These measurements were obtained using a 2.161 mm thick BK7 glass window.

window is shown in figure 2(a). The peak pair are separated by a distance $\Delta z = 1.425$ mm. The focus is then brought to each of the window interfaces in turn and the reference mirror is scanned such that it passes through the point of phase matching. The translation of the sample stage is necessary because the object is too thick for both sample surfaces to be within the Rayleigh range of the beam reflected from the focusing optic and therefore there would be insufficient reflected light if the focus were brought halfway between the surfaces. A series of interference fringes is observed in the integrated signal for each of the interfaces. The separation of the peaks of the fringe patterns ΔD, plus the confocal term Δz calculated previously, is related the thickness and the group refractive index by [16]

$$\Delta l = \Delta D + \Delta z = t \times n_{\mathrm{g}}. \tag{2}$$

An example of a pair of fringe sets acquired from the same BK7 window are shown in figure 2(b). In this example $\Delta D = 1.868$ mm, resulting in a distance $\Delta l = 3.293$ mm. The fluctuation in the signal seen between the two fringe sets, after the reference stage has translated 1 mm, is due to the motion of the sample translation stage as it moves from one surface

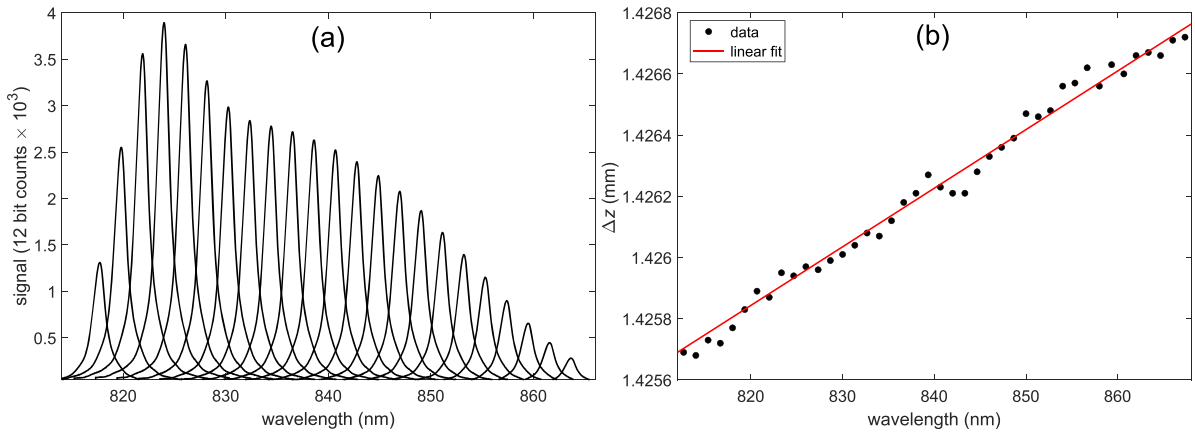

Figure 3. Plots showing (a) the confocal peaks calculated at different wavelengths for the front surface of a 2.161 mm thick BK7 window (the plot shows every second peak) and (b) the variation in Δz with wavelength from which the dispersion term $\mathrm{d}\Delta z/\mathrm{d}\nu$ is calculated. The gradient $\mathrm{d}\Delta z/\mathrm{d}\lambda$ in (b) is 19.64.

to the other. Accurate measurement of ΔD requires the calculation of the envelope of each set of interference fringes. There are several methods of calculating the fringe envelope [28] and the technique used in this work is based on the Hilbert transform [29].

The group index depends on the chromatic dispersion, given by

$$n_{\mathrm{g}}(\nu) = n_{\mathrm{p}}(\nu) + \nu \frac{\mathrm{d}n_{\mathrm{p}}(\nu)}{\mathrm{d}\nu} \tag{3}$$

where ν is the optical frequency. Therefore, n_{p} and thus Δz are functions of frequency. In the case that $NA^2 \ll 1$, the approximation given in equation (1) can be used. Substituting this and equation (2) into equation (3) yields

$$t^2 = \frac{\Delta l \Delta z}{1 - \left(\frac{\nu}{\Delta z}\frac{\mathrm{d}\Delta z}{\mathrm{d}\nu}\right)} \tag{4}$$

where $\mathrm{d}\Delta z/\mathrm{d}\nu$ is the dispersion of the confocal parameter. In general, the mathematical approximation given in equation (1) and used to derive equation (4) cannot be applied without introducing significant measurement error and a more complex polynomial solution must be used as given by [19]

$$At^6 + Bt^4 + Ct^2 = 0$$

where

$$A = \frac{\left(1-NA^2\right)^2}{\Delta z^4} + \nu^2 \frac{\left(1-NA^2\right)^2}{\Delta z^6}\left(\frac{\mathrm{d}\Delta z}{\mathrm{d}\nu}\right)^2 - 2\nu\frac{\left(1-NA^2\right)^2}{\Delta z^5}\frac{\mathrm{d}\Delta z}{\mathrm{d}\nu}$$

$$B = 2\frac{\left(1-NA^2\right)^2}{\Delta z^2}NA^2 - 2NA^2\nu\frac{\left(1-NA^2\right)}{\Delta z^3}\frac{\mathrm{d}\Delta z}{\mathrm{d}\nu}$$

$$C = NA^4 - \frac{\Delta l^2}{\Delta z^2}\left(1-NA^2\right)$$

$$D = -\Delta l^2 NA^2. \tag{5}$$

Once t has been obtained using equation (5), n_{p} and n_{g} can be calculated using equations (1) and (2). Equation (5) is used for all the refractive index and thickness calculations made in section 6.

Equation (5) is used for all the refractive index and thickness calculations made in section 6. To determine the dispersion term $\mathrm{d}\Delta z/\mathrm{d}\nu$, the acquired spectra are divided into separate regions, corresponding to different wavelength bins, and the mean signal is calculated within each. As the object scans, this yields a series of spectrally separated confocal peaks, such as those shown in figure 3(a). In this example taken from the front surface of a BK7 window, 46 different spectral regions were used in the processing yielding 46 peaks (for clarity every second peak is shown in figure 3(a)). The envelope of the peak series corresponds to the spectral profile of the source. This is done for each of the sample's surfaces and the dispersion term can be obtained by calculating Δz for each of the spectrally separated peaks, as shown in figure 3(b). The variation in Δz across the wavelength range of the spectrometer is only 1 μm, which highlights the accuracy requirements of the peak localization and positioning that is discussed further in section 5. The gradient of the linear fit in figure 3(b), $\mathrm{d}\Delta z/\mathrm{d}\lambda$ is 19.64 which corresponds to $\mathrm{d}\Delta z/\mathrm{d}\nu = -4.618 \times 10^{-17}$ ms. Using this value, along with the previously determined values for Δz and Δl, with equations (1)–(5) yields a calculated thickness $t = 2.156$ mm, and refractive indices $n_{\mathrm{p}} = 1.501$ and $n_{\mathrm{g}} = 1.527$.

3. Line-scan acquisition

Previously [20], the technique was demonstrated using single-line acquisition at a rate of 500 Hz. Whilst this is straightforward to implement and suitable for demonstration, it does not take full advantage of the acquisition rate of the camera. In a line-scan camera, the sensor consists of a single row of pixels, as opposed to a two-dimensional array as is found in conventional digital cameras. Line-scan acquisition involves capturing a series of one-dimensional exposures which are appended to form images, with the image size being defined by a

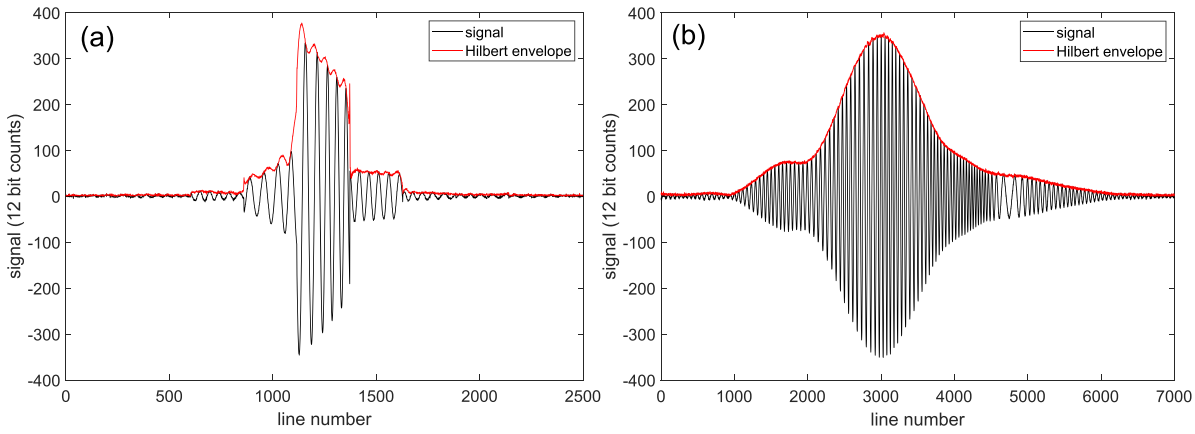

Figure 4. Plots showing (a) a low-coherence fringe envelope generated by sequential acquisition and processing of images, resulting in noticeable gaps in the signal, and (b) a similar envelope generated using a circular buffer which enables simultaneous acquisition and processing. Both examples were obtained using an image size of 250 lines and a line exposure time of 15 µs.

set number of lines. Each image therefore contains a temporal record of the signal impinging on the sensor over the acquisition period of the image. In this application each line contains a record of the source spectrum, and the images show the evolution of the spectrum as the optical components in the interferometer are scanned. The individual line acquisition rate is determined by the set exposure time, with a minimum exposure time of 15 µs corresponding to a maximum rate of ∼70 kHz.

The acquisition made during a typical measurement consists of multiple images typically containing many hundreds of lines, which is too much data to be practical to store in memory for processing after the measurement is complete. The processing that is required to derive the confocal and low-coherence data involves calculating the mean value of each spectrum. Processing an image prior to acquiring the next results in gaps in the signal, as illustrated by the example low-coherence fringe envelope shown in figure 4(a). In this example, each image consists of 250 lines acquired with a 15 µs exposure time, and a significant amount of the signal is missing. The issue is particularly noticeable in this example because of the short exposure time (high data rate), resulting in a high ratio of time when the camera is not recording to when it is, and a relatively low number of lines per image. The low-coherence measurement requires a short exposure time to resolve the interference fringes, whereas a much longer exposure time is needed for the confocal measurement. This is due to the lower levels of reflected light from a glass interface compared to a mirror. In the case of the confocal measurement the missing signal may not even be noticed, which can result in unexpected measurement errors due to peaks being unexpectedly offset by the missing measurement.

To circumvent this problem, a ring, or circular software buffer is used. The buffer consists of five arrays for image storage which work on a first-in, first-out basis. This allows for processing of stored images whilst image acquisition is continuing. Figure 4(b) shows an example of a low-coherence fringe envelope acquired using the circular buffer, and in this case, there are no gaps in the signal.

4. Measurements on a sample with multiple interfaces

The sample used in this work consists of a lens tube holding three 2.5 cm diameter BK7 glass windows with an air gap between each one. The approximate thicknesses of the windows, from front to back, are 2 mm, 1 mm, and 3 mm respectively, and the thickness of the two air gaps is approximately 2 mm. The total thickness of the sample is therefore approximately 10 mm. The lens tube is positioned in a 5-axis kinematic mount (Thorlabs K5X1), which helps facilitate accurate alignment of the optics to the beam and this is mounted on the sample arm translation stage. A schematic diagram and a photograph of the test object are shown in figures 5(a) and (b) respectively.

The variation in the positions of the two stages (sample stage 1 and reference stage 2) over the course of a typical measurement are shown in figure 6. The position values in the plot are returned from the translation stage encoders. Prior to the measurement commencing, the stages are brought to their initial positions. These are predetermined based on the location of front surface of the sample for stage 1, and the location of the first fringe envelope for stage 2. These positions are relative to the stage zeroes, which are defined by default as the centre of their 50 mm travel (−25 mm to +25 mm). The camera is initialized with the settings used for the confocal measurement, including region-of-interest, number of lines per image, and exposure time.

The confocal measurement is made by a single linear scan of stage 1 through each of the sample surfaces. This scan is highlighted in the red shaded area in figure 6. As a result of this scan a series of six peaks is observed in the reflected signal, as shown in figure 7(a). This is done over multiple wavelength bins so that the dispersion of the confocal parameter can be

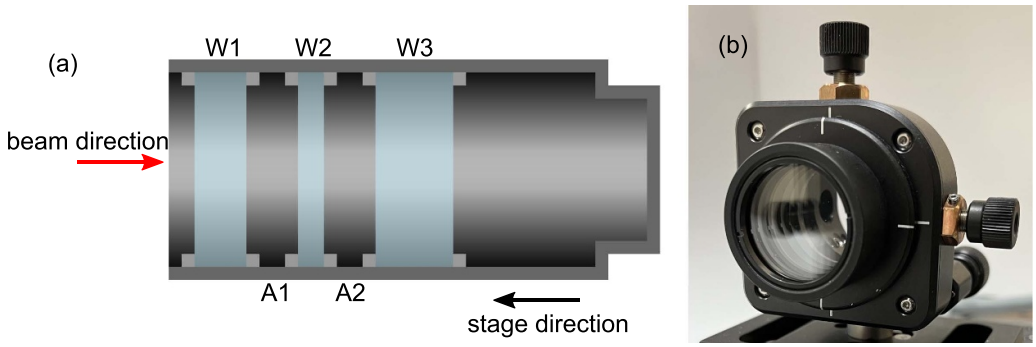

Figure 5. (a) Schematic of the 2.5 cm diameter multiple surface test object, where $W_1 - W_3$ are the three windows with nominal thicknesses of 2 mm, 1 mm, and 3 mm respectively, and A_1 and A_2 are air gaps with thicknesses of approximately 2 mm. (b) A photograph of the test object in a 5-axis kinematic mount. The total thickness of the sample from the front surface of W_1 to the rear surface of W_3 is ∼10.5 mm.

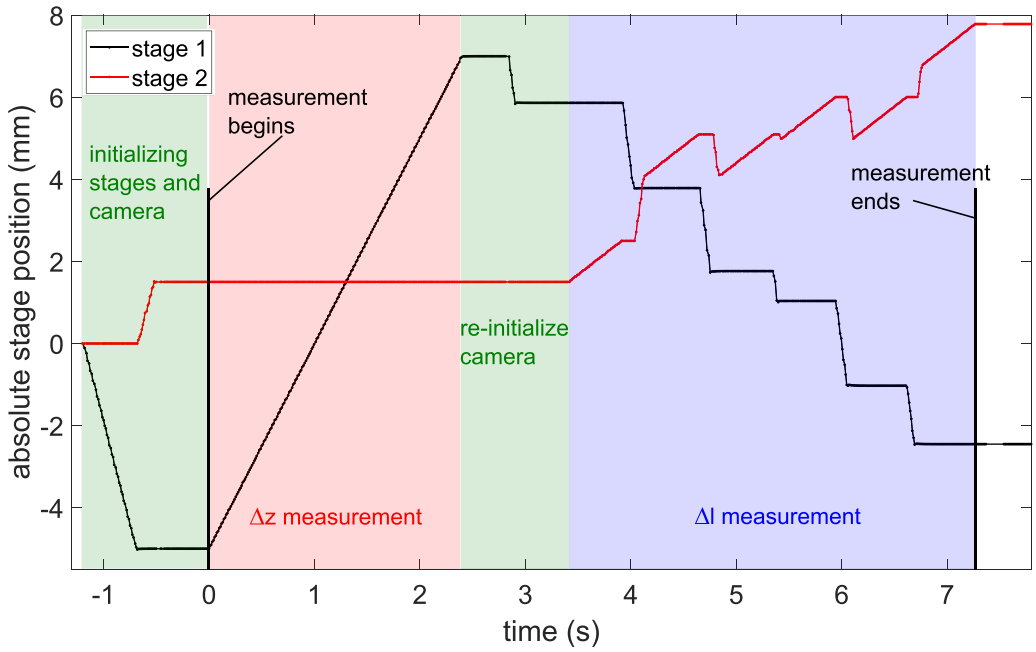

Figure 6. Plot showing the path traversed by the sample stage 1 (black) and reference mirror stage 2 (red) for a multiple surface object. The confocal (Δz) measurement (red highlight) from 0 to ∼2.4 s consists of a single 12 mm scan. The low-coherence (Δl) measurement (blue highlight) from ∼3.4 to ∼7.2 s consists of six scans of the reference mirror on stage 2 with the object (on stage 1) placed at the focus of each of the interfaces.

computed for the medium between each pair of interfaces. For the first two windows, W_1 and W_2, the variation in Δz is approximately linear with wavelength, as in the plot shown in figure 3(b). However, for the second air gap A_2 and the third window W_3, a fringe pattern is observed in the dispersion data caused by the interference of multiple reflections of light within the sample. A typical dispersion curve acquired from window W_3 is shown in figure 7(b). In this case, the gradient required to compute the dispersion term $\mathrm{d}\Delta z/\mathrm{d}\nu$ can be taken from the slope of the fringe pattern.

When making the low-coherence measurement, the reference mirror location corresponding to the point of phase matching for each individual surface is not implicitly known and is dependent on the setup of the interferometer. The initial reference stage position for each individual scan can be found by locating the phase matching point for the rear surface and calculating the locations for subsequent scans in an approximate way based on the confocal peak positions and equations (1) and (2). This requires an estimate of the refractive index of the medium between each surface. The better this estimate is, the shorter the reference mirror scan distance can be for each of the low-coherence envelopes. An example of a low-coherence measurement made with this sample is shown in figure 7(c). For this example, a refractive index estimate of 1.5 was used for the windows, and 1 for the air gaps. A scan distance of 1 mm was used for each surface. Since the refractive index of air is close to unity, the phase matching points for the surfaces either side of the air gaps are in approximately the same position, therefore the fringe envelopes associated with them are co-located in figure 7(c). Plotting the same data against image number, instead of the reference stage position, shows that there are six fringe envelopes present (figure 7(d)).

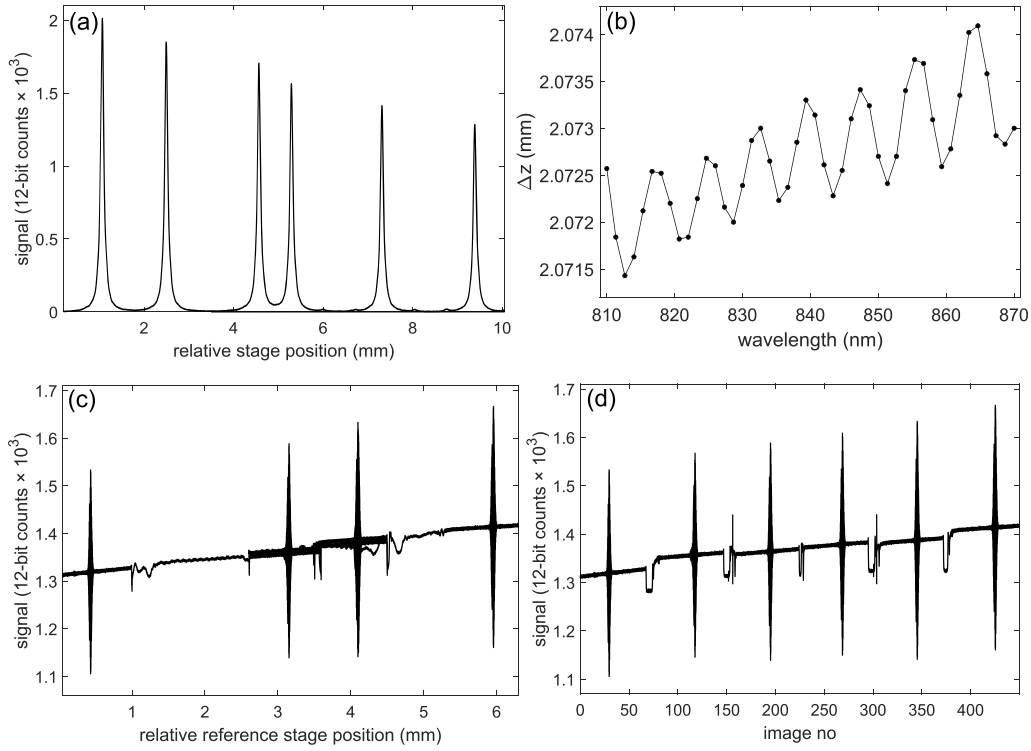

Figure 7. Confocal and low-coherence measurements made on a multiple surfaced sample: the plots show (a) the confocal peaks and (b) the dispersion curve of the third window W_3 which exhibits a fringe pattern due to multiple reflections within the sample, (c) shows the low-coherence measurement; note that the fringe envelopes associated with surfaces either side of the air gaps are co-located (at ∼3.2 mm and ∼4.1 mm), and (d) shows the low-coherence signal plotted vs image number showing that there are indeed six distinct envelopes.

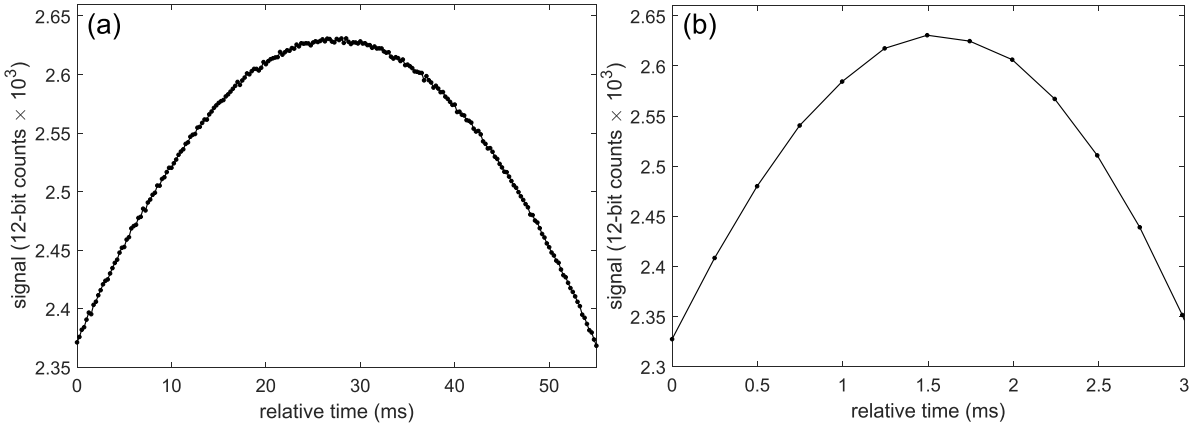

Figure 8. The top 10% of a confocal peak acquired with stage velocities of (a) 0.5 mm·s^{-1} and (b) 10 mm·s^{-1}. Both signals were acquired with the same exposure time, and hence sampling rate, of 250 μs (4 kS·s^{-1}).

5. Peak localization

Making good refractive index and thickness measurements relies on accurate peak localization. This involves peak detection to locate the position of the peaks within a dataset and establishing the stage position coinciding with each of the peaks. This section describes how these two processes are performed and the implications that increasing the stage velocity has on them.

Peak detection is performed using the 'Peak detect' function in LabVIEW which, importantly, returns peak locations at fractional indices. The function is based on a short-time quadratic fit that is applied to sections of the data [30]. The length of the section of data to which the fit is applied is determined by the 'width' parameter, which by default is set to the minimum value of 3 data-points. Setting the width at this minimum value provides the best accuracy however it can be affected by noise, with more false positives being detected in noisier signals. Increasing the width reduces the number of false peaks detected by effectively filtering the signal, which comes at the cost of reduced accuracy. Figure 8(a) shows the top 10% of a confocal peak acquired at a stage velocity of 0.5 mm·s^{-1} and

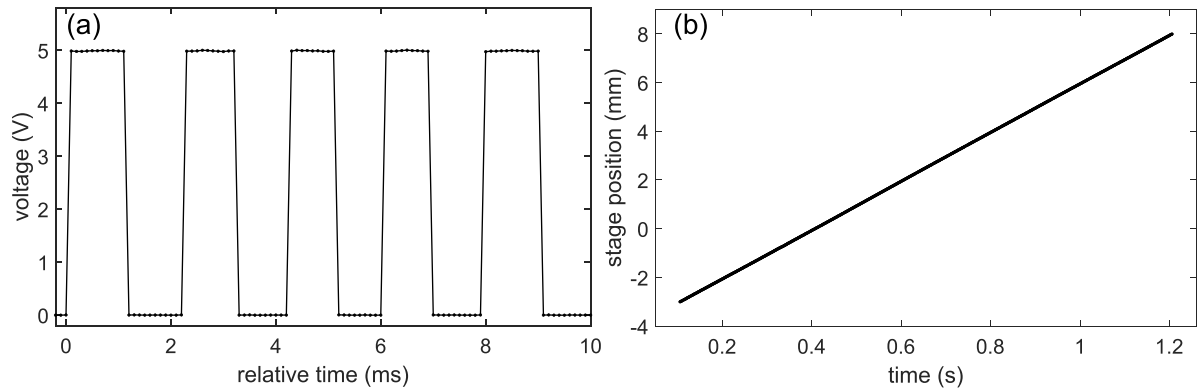

Figure 9. (a) A section of a pulse train acquired from a −3 mm to 8 mm stage translation at 10 mm·s^{-1} with a 20 µm pulse separation and (b) the variation in stage position calculated from the rising and falling edges of the pulse train.

with an exposure time of 250 µs. The amount of noise on this peak is sufficient to return numerous false positives if the minimum width were used. In comparison, the peak in figure 8(b), acquired at a stage velocity of 10 mm·s^{-1} and a 250 µs exposure time, does not resolve the noise and the lower number of datapoints means that accurate peak detection is more challenging. To deal with noise at lower stage velocities, a seven-term polynomial fit is applied to the top 50% of each peak. This is particularly important for the dispersion measurement where, due to reduced signal level at the edges of the spectral distribution (figure 3(a)), the signal-to-noise level of peaks across all the wavelength bins is not constant.

The process of calibrating the stage position for each of the peak locations begins by reading one of the digital output lines on the stage controller. This line generates a pulse train in which the pulse separation can be set to defined travel distance over a particular travel range. A section of a typical pulse train, recorded using an NI 9223 analog input module housed in a NI cDAQ-9174 chassis, is shown in figure 9(a). The pulse train, acquired at an input rate of 10 kS·s^{-1}, was set-up so that a pulse was emitted each time the translation stage made an incremental motion of 20 µm, beginning when the stage passed −3 mm and ending at 8 mm. The stage was set to travel at a velocity of 10 mm·s^{-1}. There are five pulses in the 10 ms window shown in figure 9(a) which confirms the 10 mm·s^{-1} stage velocity based on the 20 µm pulse separation. The pulses generated by the stage controller have a minimum width of 50 µs, therefore, to prevent aliasing of the pulse train, the pulse separation should not be set too low for a particular stage velocity. The higher the velocity, the smaller the pulse separation can be. The small variation in the pulsewidth from one pulse to the next in figure 9(a), is due to fluctuations in the stage velocity as it maintains a constant average velocity over the travel range.

The variation in stage position over the course of a translation is calculated from the interpolation of the rising and falling edges of the pulse train. Figure 9(b) shows this variation for a −3 mm to 8 mm translation with a 20 µm pulse separation. This data is used to calibrate the absolute stage position for each of the peaks, based on the timestamps of each of the spectrometer acquisitions corresponding to them.

Table 1. Summary of the stage velocities and the total measurement time for each of the measurement sets.

Measurement set	Stage 1 velocity	Stage 2 velocity (scan)	Measurement time
1	0.5 mm·s^{-1}	1.0 mm·s^{-1}	31.7 s
2	1.0 mm·s^{-1}	1.0 mm·s^{-1}	19.7 s
3	2.0 mm·s^{-1}	2.0 mm·s^{-1}	10.7 s
4	5.0 mm·s^{-1}	2.0 mm·s^{-1}	7.1 s
5	10 mm·s^{-1}	5.0 mm·s^{-1}	4.4 s
6	20 mm·s^{-1}	5.0 mm·s^{-1}	3.9 s

6. Refractive index and thickness measurements

The overall performance of the system was assessed at a range of different stage velocities, corresponding to different measurement times. This was done by determining the accuracy and repeatability of measurements of the refractive index and thickness of each of the components within the test sample (shown in figure 5). The instrument is used to measure Δz, ΔD, and $\mathrm{d}\Delta z/\mathrm{d}\nu$ and these parameters are used to calculate t with equation (5), which is then used to calculate n_p and n_g using equations (1) and (2). The velocity of the sample stage (stage 1) was increased from 0.5 mm·s^{-1} to 20 mm·s^{-1} in varying increments as summarised in table 1. The velocity of the reference stage (stage 2) was also increased for the low-coherence scans which further reduced the total measurement time. A set of the measured components for each of the five elements, the three windows and two air gaps, made under Measurement set four conditions is given in appendix A1 in the supplementary materials document. Refractive index and thickness measurements were made 20 times for each of the measurement sets. The measurement times in table 1 include line-scan acquisition, peak detection, and the data analysis required to derive Δz and Δl. The final refractive index and thickness calculation is done as post-process because determination of the correct dispersion gradient still requires some human interaction, particularly with noisy signals and those affected by fringing (such as in figure 7(b)). The calculation

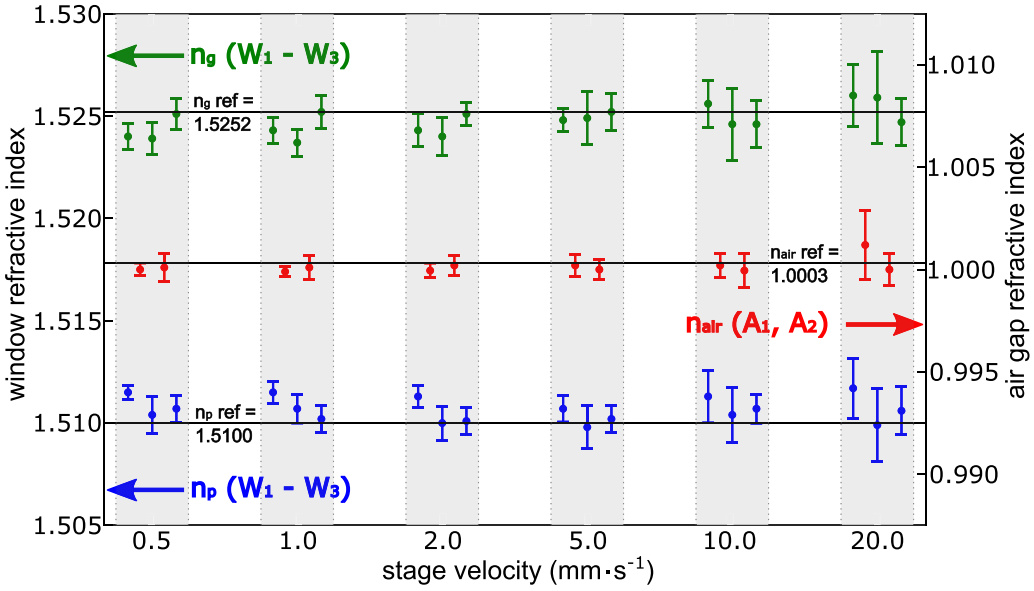

Figure 10. Refractive index measurements made at a range of stage velocities. The upper (in green) and lower (in blue) rows show measurements of n_g and n_p for the three windows ($W_1 - W_3$) respectively, and the central row in red shows measurements of the refractive index of the air gaps (A_1, A_2).

itself is fast relative to the overall measurement time (tens of milliseconds).

The refractive index measurements for each of the five elements within the sample are shown in figure 10. The data used to produce the plot is tabulated and provided in appendix A2 in the supplementary materials document. The vertical grey banding indicates that each of the data points within that particular band were acquired at the same stage velocity. Within each band are eight data-points corresponding to the measurements of n_p (shown in blue in the lower row) and n_g (shown in green in the upper row) for the three windows ($W_1 - W_3$), and the refractive index of the air gaps (shown in red in the central row). The magnitudes of the window and air gap refractive indices are provided by the left and right y-axes respectively. The air gap refractive index values are taken from the mean of n_p and n_g measurements. The error bars on each data-point correspond to the standard deviation of the 20 individual measurements. The reference refractive index values for BK7 glass at 850 nm are 1.5100 for n_p and 1.5252 for n_g [31], and 1.0003 for air [31]. These values are indicated by the black horizontal lines in figure 10.

Whilst the repeatability does reduce somewhat at higher stage velocities with, for example, a maximum standard deviation of 2.26×10^{-3} at 20 mm·s^{-1}, compared to 0.94×10^{-3} at 2.0 mm·s^{-1}, the accuracy is relatively consistent across the velocity range. The lowest accuracy measured was for window W_1 at 20 mm·s^{-1} at 0.11% and was below 0.1% for all other measurements. The measurement of n_p for W_1 was slightly overestimated at each stage velocity suggesting a systematic error, possibly due to the alignment.

The thickness measurements for each of the sample elements are shown in figure 11. The tabulated data used to produce the plot can be found in appendix A3 in the supplementary materials document. Again, the grey vertical bands indicate that all the measurement points within them were acquired at the same stage velocity. Note that the y-axis is split into regions covering each of the five different elements. The reference values for the three windows are indicated by the black horizontal lines in figure 11. These were derived from repeated measurements of the window thickness using a Mitutoyo MDH digital micrometre gauge, which has a resolution of 0.1 µm and an accuracy of 0.5 µm. The standard deviations of 10 measurements of each window are 0.61 mm, 0.57 mm, and 0.49 mm for windows $W_1 - W_3$ respectively. There are no reference thickness values for the air gaps since, whilst the retaining rings used in the construction of the sample ensure that the air gaps are approximately 2 mm, it is particularly difficult to measure the gap thickness to sufficient accuracy to provide a meaningful reference. The horizontal black dashed line shown for the two air gaps indicates the mean of the six measurement sets.

As with the refractive index measurements, there is a reduction in the repeatability as the stage velocity increases. This is to be expected given the lower resolution of the detected peaks. The smallest standard deviation is 0.55×10^{-3} mm, which was obtained for window W_2 at 1.0 mm·s^{-1}, whereas the highest is 2.26×10^{-3} mm obtained for window W_3 at 20 mm·s^{-1}. The accuracy remains good to 10 mm·s^{-1} with a percentage error below 0.08% for all windows at all velocities at 10 mm·s^{-1} and below. The accuracy does noticeably reduce at 20 mm·s^{-1} however with a maximum percentage error of 0.17% for window W_2 at 20 mm·s^{-1}.

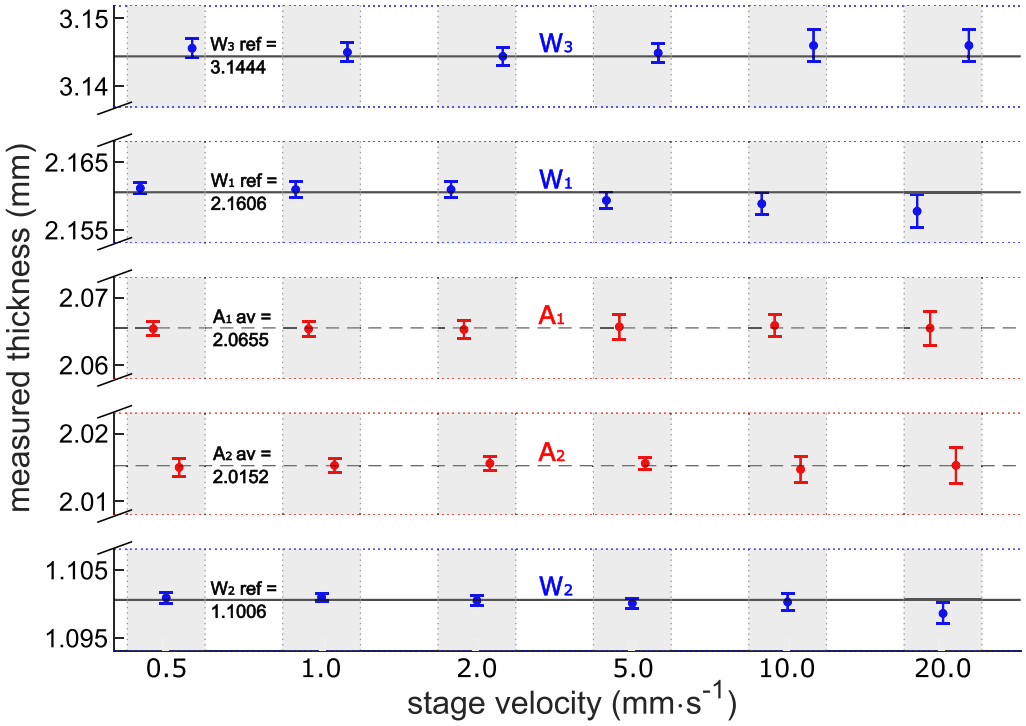

Figure 11. Thickness measurements made across a range of stage velocities. The y-axis is split to cover the ranges of the measurements for each of the five elements. The three windows ($W_1 - W_3$) are shown in blue and the two air gaps (A_1 and A_2) are shown in red.

7. Discussion and conclusion

This paper has described refractive index and thickness measurement using combined LCI and confocal scanning with an emphasis on improving the measurement speed. Reducing the measurement time by increasing translation stage velocity introduces several difficulties, such as the need for fast data acquisition and accurate peak localization, and the steps taken to mitigate these issues has been discussed. Measurements have been presented using a multi-layered sample consisting of three windows in a lens tube. The effect of translation stage velocity on the accuracy and repeatability of refractive index and thickness measurements has been investigated. Whilst there is a reduction in accuracy and repeatability at the higher stage velocities, due to a reduction in the peak resolution, a total measurement time of 4.4 s with percentage errors less than 0.1% across all three measurands n_p, n_g, and t was achieved for a total sample length of ∼10.5 mm. This represents an improvement of approximately two orders of magnitude over previously published work [20].

Alignment of the beam so that it is on axis is believed to be the main source of systematic error, and what causes the slight underestimation of n_p for window W_1. Spherical aberration in the focusing lens is also a significant source of systematic error though this is improved significantly by using OAP mirrors over comparable lens systems. The OAP mirrors themselves are difficult to align though and misalignment will introduce systematic error. The use of OAP mirrors in the instrument is described in more detail in [27]. The work described here was carried out in a laboratory and the effects of thermal variations and environmental disturbances were not noticed, though this may be an issue if the instrument were used in more difficult situations.

To make further improvements on the measurement time through greater stage velocities would ultimately require better resolution of the acquired peak data. This would require faster acquisition and better noise performance to allow shorter exposure times whilst maintaining a high signal level. Increasing the optical bandwidth of the spectrometer and source would also help as it would provide greater separation of dispersed confocal peaks making the dispersion measurement easier. In the measurements presented here the refractive index difference at the interfaces is relatively large, which means that the reflected light levels are relatively high. Making measurements on samples with much closer refractive index differences will be more challenging, and these improvements would be necessary to maintain the measurement speeds discussed here. Improvements to the measurement accuracy could be made with better peak localization. One potential way of achieving this could be to implement interferometric stage encoding [32], which can provide nano-scale position measurement. As it is remote from the stage system itself it should be easier to synchronise the interferometric position data with the spectrometer acquisitions than the pulse train technique described here.

Data availability statement

The data that support the findings of this study are openly available at the following URL/DOI: https://doi.org/10.17862/cranfield.rd.21975965.v1.

Acknowledgments

This work is dedicated to the memory of our colleague, Dr Helen Ford.

The authors would like to acknowledge support from the Engineering and Physical Sciences Research Council via Grants EP/M010473/1 and EP/H02252X/1. The authors declare that they have no competing interests.

ORCID iDs

D Francis https://orcid.org/0000-0002-8675-5134
J M Hallam https://orcid.org/0000-0002-7087-0461
R P Tatam https://orcid.org/0000-0001-9599-3639

References

[1] Yao J, Huang J, Meemon P, Ponting M and Rolland J P 2015 Simultaneous estimation of thickness and refractive index of layered gradient refractive index optics using a hybrid confocal-scan swept source optical coherence tomography system *Opt. Express* **23** 30149–64
[2] Boettcher J, Gronle M and Osten W 2017 Multi-layer topography measurement using a new hybrid single-shot technique: chromatic confocal coherence tomography (CCCT) *Opt. Express* **25** 10204–13
[3] El-Haddad M T and Tao Y K 2019 Non-contact characterization of compound optical elements using reflectance confocal microscopy, low-coherence interferometry, and computational ray-tracing *Sci. Rep.* **9** 17111
[4] Jan C-M, Liu C-S, Chen C-L and Chen Y-T 2021 Optical interference system for simultaneously measuring refractive index and thickness of slim transparent plate *Opt. Laser Eng.* **145** 14
[5] Cho S-W, Kim G H, Kim M, Shin B S and Kim C-S 2017 Line-field swept-source interferometer for simultaneous measurement of thickness and refractive index distribution *J. Lightwave Technol.* **35** 3584–90
[6] Zilio S C 2014 Simultaneous thickness and group index measurement with a single arm low-coherence interferometer *Opt. Express* **22** 27392–7
[7] Moreno-Hernández C, Monzón-Hernández D, Hernández-Romano I and Villatoro J 2015 Single tapered fiber tip for simultaneous measurements of thickness, refractive index and distance to a sample *Opt. Express* **23** 22141–8
[8] Liu C-S and Weng T-Y 2021 Thickness and refractive index measurement system for multilayered samples *IEEE Access* **9** 21474–80
[9] Park J, Bae J, Kim J-A and Jin J 2019 Physical thickness and group refractive index measurement of individual layers for double-stacked microstructures using spectral-domain interferometry *Opt. Commun.* **431** 181–6
[10] Huang D *et al* 1991 Optical coherence tomography *Science* **254** 1178–81
[11] Tearney G J, Brezinski M E, Southern J F, Bouma B E, Hee M R and Fujimoto J G 1995 Determination of the refractive index of highly scattering human tissue by optical coherence tomography *Opt. Lett.* **20** 2258–60
[12] Fukano T and Yamaguchi I 1996 Simultaneous measurement of thicknesses and refractive indices of multiple layers by a low-coherence confocal interference microscope *Opt. Lett.* **21** 1942–4
[13] Ohmi M, Shiraishi T, Tajiri H and Haruna M 1997 Simultaneous measurement of refractive index and thickness of transparent plates by low coherence interferometry *Opt. Rev.* **4** 507–15
[14] Fukano T and Yamaguchi I 1999 Separation of measurement of the refractive index and the geometrical thickness by use of a wavelength-scanning interferometer with a confocal microscope *Appl. Opt.* **38** 4065–73
[15] Ohmi M, Ohnishi Y, Yoden K and Haruna M 2000 *In vitro* simultaneous measurement of refractive index and thickness of biological tissue by the low coherence interferometry *IEEE Trans. Biomed. Eng.* **47** 1266–70
[16] Haruna M, Ohmi M, Mitsuyama T, Tajiri H, Maruyama H and Hashimoto M 1998 Simultaneous measurement of the phase and group indices and the thickness of transparent plates by low-coherence interferometry *Opt. Lett.* **23** 966–8
[17] Maruyama H, Mitsuyama T, Ohmi M and Haruna M 2000 Simultaneous measurement of refractive index and thickness considering chromatic dispersion of index *Opt. Rev.* **7** 468–72
[18] Maruyama H, Inoue S, Mitsuyama T, Ohmi M and Haruna M 2002 Low-coherence interferometer system for the simultaneous measurement of refractive index and thickness *Appl. Opt.* **41** 1315–22
[19] Kim S, Na J, Kim M J and Lee B H 2008 Simultaneous measurement of refractive index and thickness by combining low-coherence interferometry and confocal optics *Opt. Express* **16** 5516–26
[20] Francis D, Ford H D and Tatam R P 2018 Spectrometer-based refractive index and dispersion measurement using low-coherence interferometry with confocal scanning *Opt. Express* **26** 3604–17
[21] Ohmi M, Nishi H, Konishi Y, Yamada Y and Haruna M 2004 High-speed simultaneous measurement of refractive index and thickness of transparent plates by low-coherence interferometry and confocal optics *Meas. Sci. Technol.* **15** 1531–5
[22] Park S J, Park K S, Kim Y H and Lee B H 2011 Simultaneous measurements of refractive index and thickness by spectral-domain low coherence interferometry having dual sample probes *IEEE Photonics Technol. Lett.* L **23** 1076–8
[23] Kuo W-C, Bou Y-K and Lai C-M 2013 Simultaneous measurement of refractive index and thickness of transparent material by dual-beam confocal microscopy *Meas. Sci. Technol.* **24** 075003
[24] Szarlan T, Gibson D, Wei X and Ignatovich F 2020 Accurate measurements of phase refractive index of soft contact lenses *Opt. Express* **28** 10818–35
[25] Na J, Choi H Y, Choi E S, Lee C S and Lee B H 2009 Self-referenced spectral interferometry for simultaneous measurements of thickness and refractive index *Appl. Opt.* **48** 2461–7
[26] Moore E D and McLeod R R 2011 Phase-sensitive swept-source interferometry for absolute ranging with application to measurements of group refractive index and thickness *Opt. Express* **19** 8117–26

[27] Ford H D, Francis D, Hallam J M and Tatam R P 2019 Influence of aberrations on confocal-based remote refractive index measurements *Appl. Opt.* **58** 6474–85
[28] Liu P, Groves R M and Benedictus R 2013 Signal processing in optical coherence tomography for aerospace material characterization *Opt. Eng.* **52** 033201
[29] Pavliček P and Michálek V 2012 White-light interferometry—envelope detection by Hilbert transform and influence of noise *Opt. Laser. Eng.* **50** 1063–8
[30] Anon A Peak detection using LabVIEW and Measurement Studio 2020 *ni.com* (available at: www.ni.com/en-gb/support/documentation/supplemental/06/peak-detection-using-labview-and-measurement-studio.html) (Accessed 10 June 2022)
[31] Polyanskiy M N Refractive index database (available at: https://refractiveindex.info) (Accessed 24 November 2022)
[32] Wiseman K B, Kissinger T and Tatam R P 2021 Three-dimensional interferometric stage encoder using a single access port *Opt. Laser. Eng.* **137** 106342

https://dspace.org/

Low-coherence and broadband confocal refractometry: reducing the measurement time

Francis, Daniel; Hallam, Jonathan M.; Tatam, Ralph P.

2023-12-01
IOP Publishing
https://doi.org/10.1088/1361-6501/acf334
Francis D, Hallam JM, Tatam RP. (2023) Low-coherence and broadband confocal refractometry: reducing the measurement time. Measurement Science and Technology, Volume 34, Issue 12, December 2023, Article Number 125204

Downloaded from a DSpace repository. https://dspace.org/